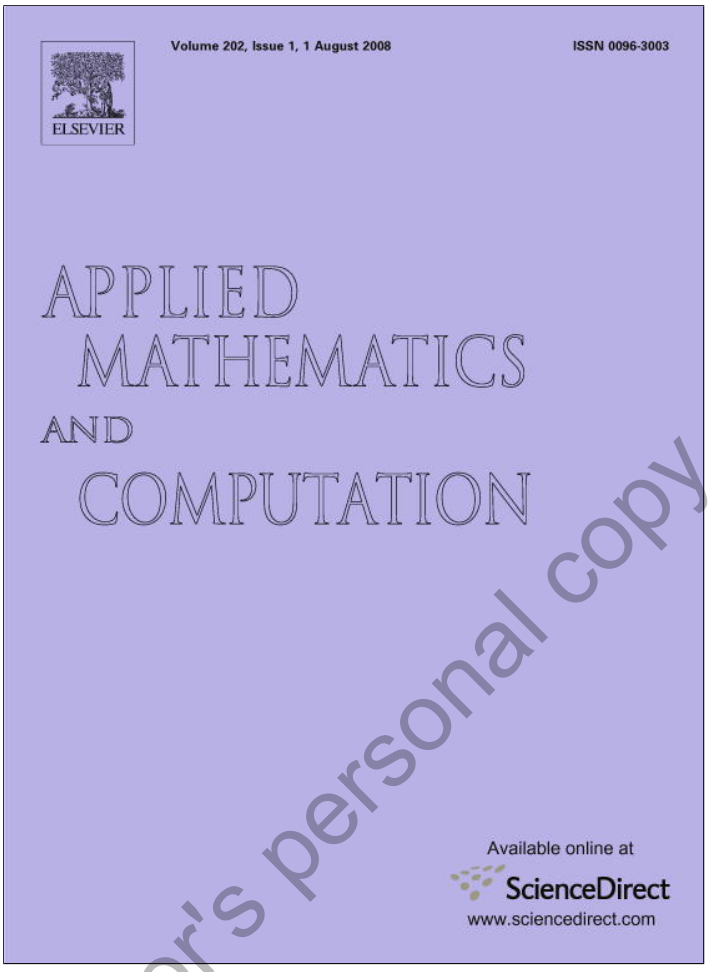

Available online at www.sciencedirect.com
ScienceDirect
Applied Mathematics and Computation 202 (2008) 146–161
APPLIED MATHEMATICS AND COMPUTATION
www.elsevier.com/locate/amc

Numerical stabilities and boundary conditions in time-domain Eulerian simulations of acoustic wave propagations with and without background flow

Z.C. Zheng *, W. Li

Department of Mechanical and Nuclear Engineering, Kansas State University, Manhattan, KS 66506, United States

Abstract

A thorough numerical analysis is performed for time-domain simulation of acoustic wave propagations in the atmosphere, with the ground modeled as a porous medium. Two types of computational grid arrangement for the simulation, i.e., the staggered grid and the collocated grid, are considered. It is proved that the computational schemes based on these two grids are identical under certain finite differencing procedures. The numerical stability analysis is studied that applies to both of the grids. Non-reflecting, absorbing boundary conditions are used at the free-space boundary. Simulations on the collocated grid are then carried out for a model problem of sound propagation in the air/ground to confirm the equivalency of the two grids and to investigate the effectiveness of non-reflecting boundary conditions. The results are compared with the data in the literature and with bench-mark simulation, and very good agreements have been achieved.

Keywords: Eulerian simulation; Acoustic propagations; Non-reflecting boundary conditions

1. Introduction

With the advent of computing power, time-domain (TD) acoustic simulations have become feasible. The primary advantage of the TD technique is its ability to accommodate complicated geometries and background fluid flow [1–3]. However, there are several issues related to the TD methods that need to be resolved. In this paper, we demonstrate the procedures to address numerical stabilities and boundary conditions in the TD numerical simulations, using a simple model problem and a typical second-order numerical scheme.

Two different types of spatial grid arrangement for TD acoustic simulations can be used: the collocated grid and the staggered grid. Most of the TD simulations in the literature are on the staggered grid, e.g. [1–3]. The advantage of staggered grid is that it avoids oscillatory solutions from the spatial central differencing [4], particularly for equations with dominant first-order derivatives. On the other hand, the drawback of staggered grid is tedious grid indexing when there are complicated geometries involved and non-uniform grids are

* Corresponding author.
E-mail address: zzheng@ksu.edu (Z.C. Zheng).

0096-3003/$ - see front matter © 2008 Elsevier Inc. All rights reserved.
doi:10.1016/j.amc.2008.01.028

required to accommodate the boundary geometries. However, complicated geometries are those situations when the TD simulations are particularly useful. Therefore, in this paper, the collocated grid mesh is mostly used. Yet, we prove that in the second-order computational schemes used in this paper, these two grid arrangements are virtually the same. Furthermore, in the test problem studied in this paper, numerical solutions from the collocated grid are compared with those from the staggered grid to show their equivalency.

In the TD methods, time marching is used in the numerical simulation. A physical restriction on the size of time marching is from the maximum frequency to be resolved by the simulation following the Nyquist rule. An additional restriction is from numerical stability during the time marching. Although, for simulating high-frequency signals, the Nyquist rule is usually more restrictive than the stability condition, the stability requirement is important when only low-frequency results are need. Nevertheless, the stability condition needs to be known when designing any numerical scheme. The stability conditions are discussed for the second-order schemes used in the wave propagation equations in the air under both homogeneous (without the ambient flow) and inhomogeneous (with the ambient flow) conditions and in the ground porous medium.

In computational of acoustic wave propagation, boundary conditions are usually needed at the interface between different media and at the free-space, open boundary. Physically, in TD simulations, surface impedances need not be specified at the interface between different media in TD simulations because they can be numerically calculated if the physical properties of the media are known. Surface impedances are usually specified in the frequency domain anyway. (Problems of frequency-dependent properties have been discussed in the literature such as [5] and are not explored in this paper.) For the open boundary, the issue of numerical wave reflection at the free-space boundaries is discussed here. The approximation of wave equations as a treatment at the free-space boundary [6–9] and the absorbing-layer methods [3,10,11] are the two primary types of free-space boundary conditions. In this study, several non-reflecting boundary conditions have been tested under both homogeneous and inhomogeneous environment, along with an investigation of a combination of these boundary conditions for enhancing the non-reflecting effect. Comparisons are made among the results by using these boundary conditions.

2. Description of the test problem

The test problem is selected to be the same as that in [2] and is illustrated in Fig. 1. The domain is composed of air over the ground modeled as a rigid-frame porous medium. The coordinate system is set up where the y-direction is the lateral direction parallel to the ground plane and the z-direction is the vertical direction perpendicular to the ground. The size of the domain may vary depending on the conditions in different test cases. In the z-direction, $z \in [0, z_{\max}]$ is in the air and $z \in [z_g, 0]$ in the ground porous medium. In some cases, from $z_{\max}$ to z_e, there is an absorbing layer added for simulating the unbounded, free-space boundary condition, which will be discussed in Section 5. The background shear flow, $\mathbf{u}_{\text{av}} = V_{\text{av}}(z)\mathbf{j}$, is considered a flow in the y-direction only in this study.

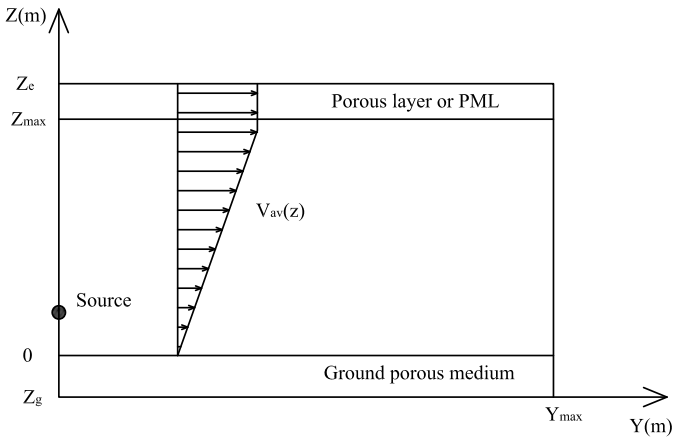

Fig. 1. Illustration of the test problem and the coordinate system.

The sound source is in the air, as illustrated in Fig. 1. The source is a pressure pulse in the form of

$$p(\mathbf{r}, t = 0) = \exp(-40r^2), \quad \mathbf{u} = 0, \tag{1}$$

where r is the distance from the source position with p in Pa and r in m.

By neglecting the higher-order acoustic terms, the linearized acoustic propagation equations in the air are

$$\frac{\partial \mathbf{u}}{\partial t} + (\mathbf{u}_{\mathrm{av}} \cdot \nabla)\mathbf{u} + (\mathbf{u} \cdot \nabla)\mathbf{u}_{\mathrm{av}} = -\alpha_{\mathrm{av}} \nabla p - \alpha \nabla p_{\mathrm{av}}, \tag{2}$$

$$\frac{\partial p}{\partial t} + \mathbf{u}_{\mathrm{av}} \cdot \nabla p + \mathbf{u} \cdot \nabla p_{\mathrm{av}} = -\gamma p \nabla \cdot \mathbf{u}_{\mathrm{av}} - \gamma p_{\mathrm{av}} \nabla \cdot \mathbf{u}. \tag{3}$$

In the above equations, the total velocity and pressure are $\mathbf{u}_{\mathrm{av}} + \mathbf{u}$ and $p_{\mathrm{av}} + p$, respectively. This kind of notations is adopted to avoid having the usual prime sign on the fluctuation part of all the variables. Therefore, $\mathbf{u}_{\mathrm{av}}$, p_{av} and α_{av} represent, respectively, velocity, pressure and specific volume of the time-averaged background, $\mathbf{u}$, p and α are their corresponding acoustic fluctuations, and γ is the specific-heat ratio. The acoustic fluctuation of specific volume is related to the pressure fluctuation with an isentropic relation:

$$\alpha = -\frac{p}{\gamma p_{\mathrm{av}} \rho_{\mathrm{av}}}. \tag{4}$$

Parameters used for the cases in this paper are: $p_{\mathrm{av}} = 100\,\mathrm{kPa}$, $\gamma = 1.4$, the speed of sound in the air $c = 340\,\mathrm{m/s}$, and $c^2 = \gamma p_{\mathrm{av}} \alpha_{\mathrm{av}}$. The background velocity is either zero for the homogeneous case or in the form of $\mathbf{u}_{\mathrm{av}} = bz\mathbf{j}$.

For acoustic waves in the ground porous medium, sound wave propagations follow the Zwikker–Kosten [12] equation

$$\frac{\partial \mathbf{u}}{\partial t} = -\frac{\Omega}{c_s} \alpha_{\mathrm{av}} (\nabla p + \sigma \mathbf{u}), \tag{5}$$

and the pressure equation [13]

$$\frac{\partial p}{\partial t} = -\frac{\gamma p_{\mathrm{av}}}{\Omega} \nabla \cdot \mathbf{u}. \tag{6}$$

In Eqs. (5) and (6), the porosity $\Omega = 0.3$, the porous medium structure factor $c_s = 3$, and the flow resistivity $\sigma = 10\,\mathrm{kPa\,s\,m^{-2}}$.

3. Numerical schemes

In the following discussions, for simplicity, we only consider two-dimensional (y–z plane) cases with $u = 0$. Also we restrict our discussions to second-order accurate schemes. Two types of numerical schemes are considered in this paper, one based on a staggered grid and the other on a collocated grid. The two-dimensional staggered and collocated grid meshes discussed in this paper are illustrated in Fig. 2.

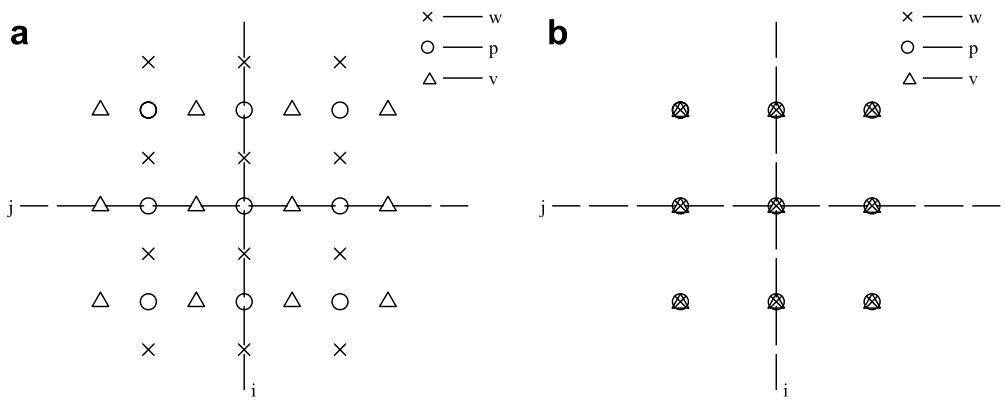

Fig. 2. Illustration of (a) the staggered grid mesh and (b) the collocated grid mesh, used in this paper.

For the ease of discussion of the numerical schemes, both the equations in the air, Eqs. (2) and (3), and the equations in the porous medium, Eqs. (5) and (6), can be written in a general format of

$$\frac{\partial \mathbf{u}}{\partial t} = P(\partial \mathbf{u}, \partial p, \mathbf{u}, p), \tag{7}$$

$$\frac{\partial p}{\partial t} = Q(\partial \mathbf{u}, \partial p, \mathbf{u}, p), \tag{8}$$

where P and Q are linear operators, and "∂" means any first-order spatial derivatives.

We define some spatial finite difference operators before discussing the two numerical schemes:

$$\delta_f u = \frac{u_{i+1} - u_i}{\Delta x_i}, \quad \delta_b u = \frac{u_i - u_{i-1}}{\Delta x_i}, \quad \text{and} \quad \delta_c u = \frac{u_{i+1/2} - u_{i-1/2}}{\Delta x_i}. \tag{9}$$

The first discretization scheme is on a staggered grid, similar to the scheme in [2]. The two-step time marching is

$$\frac{p^{n+1} - p^n}{\Delta t} = Q(\delta_c \mathbf{u}^n, \delta_c p^n, \mathbf{u}^n, p^n), \tag{10}$$

$$\frac{\mathbf{u}^{n+1} - \mathbf{u}^n}{\Delta t} = P(\delta_c \mathbf{u}^n, \delta_c p^{n+1}, \mathbf{u}^n, p^{n+1}), \tag{11}$$

where each of the variables is specified at its corresponding staggered grid location.

The second discretization scheme is on a collocated grid. With second order accuracy, the two-step time marching is

$$\frac{p^{n+1} - p^n}{\Delta t} = Q(\delta_f \mathbf{u}^n, \delta_b p^n, \mathbf{u}^n, p^n), \tag{12}$$

$$\frac{\mathbf{u}^{n+1} - \mathbf{u}^n}{\Delta t} = P(\delta_f \mathbf{u}^n, \delta_b p^{n+1}, \mathbf{u}^n, p^{n+1}), \tag{13}$$

where each of the variables is specified at its corresponding collocated grid location. Sparrow and Raspet [14] employed a similar concept in the computation of propagation of spark pulses.

Notice the finite differencing used in the two schemes. On the staggered grid in Eqs. (10) and (11), only central differencing is used. On the collocated grid in Eqs. (12) and (13), the pressure derivatives are taken using backward differencing while the velocity derivatives are using forward differencing. The alternation between forward and backward differencing for pressure and velocity results in the same second-order accurate scheme as using the central differencing with the staggered grid, which can be shown using a 1D model problem in the following discussion.

Consider a 1D problem in the y-direction. In the air, assume a constant-speed cross wind in the y direction, V_{av}, and a constant background pressure field p_{av}. Then, Eqs. (2) and (3) become

$$\frac{\partial v}{\partial t} + V_{\text{av}} \frac{\partial v}{\partial y} = -\alpha_{\text{av}} \frac{\partial p}{\partial y}, \tag{14}$$

$$\frac{\partial p}{\partial t} = V_{\text{av}} \frac{\partial p}{\partial y} - \gamma p_{\text{av}} \frac{\partial v}{\partial y}. \tag{15}$$

In the porous medium, from Eqs. (5) and (6), we have

$$\frac{\partial v}{\partial t} = -\frac{\Omega}{c_s} \alpha_{\text{av}} \left(\frac{\partial p}{\partial y} + \sigma v \right), \tag{16}$$

$$\frac{\partial p}{\partial t} = -\frac{\gamma p_{\text{av}}}{\Omega} \frac{\partial v}{\partial y}. \tag{17}$$

Next, we write out the discretized forms of these equations using the two different schemes in Eqs. (10)–(13), in order to identify their equivalency.

3.1. Discretized equations for the staggered-grid scheme

For the staggered-grid scheme represented in Eqs. (10) and (11), the discretized equations in the air, Eqs. (14) and (15), become

$$v_{j-1/2}^{n+1} - v_{j-1/2}^{n} + V_{\mathrm{av}} \frac{\Delta t}{\Delta y}(v_j^n - v_{j-1}^n) = -\alpha_{\mathrm{av}} \frac{\Delta t}{\Delta y}(p_j^{n+1} - p_{j-1}^{n+1}) \tag{18}$$

and

$$p_j^{n+1} - p_j^n + V_{\mathrm{av}} \frac{\Delta t}{\Delta y}(p_{j+1/2}^n - p_{j-1/2}^n) = -\gamma p_{\mathrm{av}} \frac{\Delta t}{\Delta y}(v_{j+1/2}^n - v_{j-1/2}^n). \tag{19}$$

Notice that on the staggered grid, v is evaluated at a half grid shifted ahead of the corresponding p. By combining the two-equation scheme of the above two equations, a discretized equation for v only can be obtained as

$$\begin{aligned} &v_{j-1/2}^{n+1} - 2v_{j-1/2}^{n} + v_{j-1/2}^{n-1} + 2V_{\mathrm{av}} \frac{\Delta t}{\Delta y}(v_j^n - v_{j-1}^n - v_j^{n-1} + v_{j-1}^{n-1}) + V_{\mathrm{av}}^2 \frac{(\Delta t)^2}{(\Delta y)^2}(v_{j+1/2}^{n-1} - 2v_{j-1/2}^{n-1} + v_{j-3/2}^{n-1}) \\ &- c^2 \frac{(\Delta t)^2}{(\Delta y)^2}(v_{j+1/2}^{n} - 2v_{j-1/2}^{n} + v_{j-3/2}^{n}) = 0. \end{aligned} \tag{20}$$

Since all of the v are evaluated on the half-shifted grids, we need the second-order interpolation

$$v_j = \frac{v_{j+1/2} + v_{j-1/2}}{2}, \tag{21}$$

which is equivalent to evaluating $p_{j+1/2}$ in Eq. (19) as

$$p_{j+1/2} = \frac{p_{j+1} + p_{j-1}}{2}, \tag{22}$$

so that Eq. (20) becomes

$$\begin{aligned} &v_{j-1/2}^{n+1} - 2v_{j-1/2}^{n} + v_{j-1/2}^{n-1} + V_{\mathrm{av}} \frac{\Delta t}{\Delta y}(v_{j+1/2}^n - v_{j-3/2}^n - v_{j+1/2}^{n-1} + v_{j-3/2}^{n-1}) + V_{\mathrm{av}}^2 \frac{(\Delta t)^2}{(\Delta y)^2}(v_{j+1/2}^{n-1} - 2v_{j-1/2}^{n-1} + v_{j-3/2}^{n-1}) \\ &- c^2 \frac{(\Delta t)^2}{(\Delta y)^2}(v_{j+1/2}^{n} - 2v_{j-1/2}^{n} + v_{j-3/2}^{n}) = 0. \end{aligned} \tag{23}$$

Following a similar procedure, the equations in the porous medium, Eqs. (16) and (17), can be discretized and combined into one equation for v, to be

$$v_{j-1/2}^{n+1} - 2v_{j-1/2}^{n} + v_{j-1/2}^{n-1} + \beta(v_{j-1/2}^{n} - v_{j-1/2}^{n-1}) - \frac{c_p^2(\Delta t)^2}{(\Delta y)^2}(v_{j+1/2}^{n} - 2v_{j-1/2}^{n} + v_{j-3/2}^{n}) = 0, \tag{24}$$

where

$$\beta = \Omega \alpha_{\mathrm{av}} \sigma \Delta t / c_s, \quad c_p = c/\sqrt{c_s}.$$

3.2. Discretized equations for the collocated-grid scheme

For the collocated-grid scheme represented in Eqs. (12) and (13), the discretized equations in the air become

$$v_j^{n+1} - v_j^n + V_{\mathrm{av}} \frac{\Delta t}{\Delta y}(v_{j+1}^n - v_j^n) = -\alpha_{\mathrm{av}} \frac{\Delta t}{\Delta y}(p_j^{n+1} - p_{j-1}^{n+1}) \tag{25}$$

and

$$p_j^{n+1} - p_j^n + V_{\mathrm{av}} \frac{\Delta t}{\Delta y}(p_j^n - p_{j-1}^n) = -\gamma p_{\mathrm{av}} \frac{\Delta t}{\Delta y}(v_{j+1}^n - v_j^n). \tag{26}$$

By combining the two-equation scheme of the above two equations, a discretized equation for v only can be obtained as

$$v_j^{n+1} - 2v_j^n + v_j^{n-1} + V_{\text{av}}\frac{\Delta t}{\Delta y}(v_{j+1}^n - v_{j+1}^{n-1} - v_{j-1}^n + v_{j-1}^{n-1}) + V_{\text{av}}^2\frac{(\Delta t)^2}{(\Delta y)^2}(v_{j+1}^{n-1} - 2v_j^{n-1} + v_{j-1}^{n-1}) - c^2\frac{(\Delta t)^2}{(\Delta z)^2}(v_{j+1}^n - 2v_j^n + v_{j-1}^n) = 0. \tag{27}$$

Similarly in the porous medium, the combined equation for v is

$$v_j^{n+1} - 2v_j^n + v_j^{n-1} + \beta(v_j^n - v_j^{n-1}) - \frac{c_p^2(\Delta t)^2}{(\Delta y)^2}(v_{j+1}^n - 2v_j^n + v_{j-1}^n) = 0. \tag{28}$$

By comparing the discretized forms in Eqs. (23) and (27) and in Eqs. (24) and (28), it is ostensible that the discretized equations on the collocated grid are equivalent to those on the staggered grid, by only shifting half of the grid index number. That is because alternating between forward and backward differencing for pressure and velocity for the collocated scheme results in the same combined equation as that for the staggered grid scheme with central differencing, both in the air and in the porous medium. It also shows that both of the schemes are central differencing in time and space, achieving a second-order accuracy in time and space.

4. Stability analysis

Here we also consider the 1D problem represented by Eqs. (14)–(17) to investigate the numerical stability of the computational schemes.

In the air, Eqs. (14) and (15) can be combined as

$$\left(\frac{\mathrm{D}}{\mathrm{D}t} + c\frac{\partial}{\partial y}\right)\left(\frac{\mathrm{D}}{\mathrm{D}t} - c\frac{\partial}{\partial y}\right)v = 0, \tag{29}$$

where

$$\frac{\mathrm{D}}{\mathrm{D}t} \equiv \frac{\partial}{\partial t} + V_{\text{av}}\frac{\partial}{\partial y}.$$

The discretized equation for v, Eq. (23) or Eq. (27), behaves as a second-order scheme with central differencing both in time and space, which is a leap-frog scheme for the wave equation [15]. Therefore the stability condition is

$$v \leqslant 1, \tag{30}$$

where, in the case of Eq. (29),

$$v = \max\left\{|c + V_{\text{av}}|\frac{\Delta t}{\Delta y}, |c - V_{\text{av}}|\frac{\Delta t}{\Delta y}\right\}.$$

In the ground porous medium, since the simple wave-equation operator is not applicable when $\beta \neq 0$ for the porous medium equations, Eqs. (16) and (17), the von Neumann stability analysis is used to analyze the stability condition for the v equation in the porous medium, Eq. (28). The eigenvalues of G ($\epsilon_j^n = G^n \cdot \mathrm{e}^{\mathrm{I}\cdot j\cdot\theta}$, $\theta = k\Delta y$, $\mathrm{I} = \sqrt{-1}$, k is the wave number) are obtained from

$$G^2 + (\gamma^2 + \beta - 2)G + (1 - \beta) = 0, \tag{31}$$

where $\gamma = 2c_p \sin(\theta/2)\Delta t/\Delta y$. Therefore

$$G = \frac{1}{2}[-(\gamma^2 + \beta - 2) \pm \sqrt{\chi}], \tag{32}$$

where

$$\chi = (\gamma^2 + \beta - 2)^2 - 4(1 - \beta).$$

To satisfy the stability condition, $|G| \leqslant 1$, it can be shown that

$$0 \leqslant \beta \leqslant 2 \quad \text{for } \chi \leqslant 0,$$

and

$$0 < 4\left(c_p \frac{\Delta t}{\Delta y}\right)^2 \leqslant 4 - 2\beta \quad \text{for } \chi > 0.$$

Combining these restrictions leads to the following condition:

$$c_p \frac{\Delta t}{\Delta y} \leqslant \sqrt{1 - \beta/2}, \quad \text{and} \quad 0 \leqslant \beta < 2. \tag{33}$$

Clearly, when the resistivity $\sigma \to 0$ or $\beta \to 0$, Eq. (33) reduces to the stability criterion for the second-order explicit leap-frog scheme of a wave equation.

Hence, using Eq. (33), the stability condition can be determined from the following expression when simulating wave propagations inside the porous medium

$$c_p \frac{\Delta t}{\Delta y} \leqslant 4 c_p c_s \frac{1}{\sqrt{16 c_p^2 c_s^2 + (\Delta y \Omega \alpha_{\text{av}} \sigma)^2} + \Delta y \Omega \alpha_{\text{av}} \sigma}. \tag{34}$$

It can be seen when the resistivity, σ, is large, the time step has to be very small to satisfy the stability condition, with the extreme condition that if $\sigma \to \infty$, the time step becomes zero.

It is also noted that when $V_{\text{av}} \to 0$ for the equation in the air and $\sigma \to 0$ for the equation in the porous medium, both of the equations reduce to a standard wave equation with a speed of sound of c in the air and c_p in the porous medium. The stability condition for both of the equations using a scheme with second-order accuracy in time and space is the same as that of a wave equation using the leap-frog scheme.

Combining the stability requirement from both Eqs. (30) and (34), the restriction on the time step for the entire problem becomes

$$\Delta t \leqslant \min \left\{ \frac{\Delta y}{|c + V_{\text{av}}|}, \frac{\Delta y}{|c - V_{\text{av}}|}, \frac{4 c_s \Delta y}{\sqrt{16 c_p^2 c_s^2 + (\Delta y \Omega \alpha_{\text{av}} \sigma)^2} + \Delta y \Omega \alpha_{\text{av}} \sigma} \right\}. \tag{35}$$

5. Non-reflecting boundary conditions

Constructing a non-reflecting boundary condition to represent a free-space boundary is still a challenging problem. In this study, we compare several cases of different boundary conditions to test the effectiveness of non-reflecting boundary conditions implemented in the simulation. We have investigated a simple absorbing layer, the perfectly-matched layer (PML), characteristic methods, and a combination of the absorbing layer or a PML and characteristic methods. The results using these boundary conditions are compared with analytical solutions in the literature or a benchmark result of a large-domain simulation. The development and the merit of each of the methods is in the corresponding literature and readers are referred to these original works. Here we concentrate on the implementation of these methods and discussions of the results from the simulation of the test problem.

The test problem for investigating free-space boundary conditions is selected similar to the pulsed sound source in air/ground problem described in [2], for the purpose of comparing our results with those in [2]. All the cases are computed using the collocated grid. The values of the parameters are listed in Section 2. As shown in Fig. 1, the sound pulse is located 0.5 m above the ground surface at time zero, with $p = \exp(-40r^2)$ where r is the distance from the source position with p in Pa and r in m. The computational domain is arranged in the y–z plane, with $y \in [0, 7]$ (in m) or $y \in [0, 12]$, and with $z \in [0, 4]$ for the air portion and $z \in [-1, 0]$ for the ground porous medium.

The effect of non-reflecting boundary conditions is tested at the top boundary. Since the sound source is located at $(0, 0.5)$, the incident angle of the sound wave remains zero at $y = 0$ where only the rigid boundary condition is necessary. At $y_{\max}$, the rigid boundary is again used if we limit the total simulation time so that the sound wave may not reach the right boundary at the end of the simulation. For simulation time up to 20 ms, $y_{\max} = 7$ is used, and for simulation up to 34 ms, $y_{\max} = 12$. Of course, non-reflecting boundary conditions can be easily employed at $y_{\max}$ if longer time simulations are desired. In this study we only select the top boundary to test the boundary condition behavior. Furthermore, wherever the rigid boundary condition is specified, it is $u_n = 0$ and $\partial p/\partial n = 0$ where n means the normal direction of the boundary at which the rigid boundary condition is employed.

5.1. A simple porous absorbing layer

The first method is simply to add a layer of porous medium as an absorbing layer at the top of the domain. The added absorbing layer has a thickness of $(z_e - z_{\max})$ m (for $z \in [z_{\max}, z_e]$), with a flow resistivity of σ_e (to be determined in different simulation cases) and $c_s = \Omega = 1$, and other properties the same as the ground porous medium stated in Section 2. At the end of the absorbing layer $(z = z_e)$, either the rigid boundary condition or the characteristic boundary condition (to be discussed later) is specified and results are compared.

High resistivity may not effectively reduce reflection at the air/absorbing-layer interface, but the thickness of the absorbing layer can be small because the wave is quickly damped inside a high resistivity layer. On the other hand, low resistivity can effectively reduce the reflection at the air/absorbing-layer interface, but the thickness of the absorbing layer has to be large in order to damp the wave inside the absorbing layer. Otherwise the remaining wave can reflect at the end of the absorbing layer and still propagate back to the medium domain, although implementing a radiative boundary condition at the end may reduce such reflections. Therefore, the selection of σ_e values is to accommodate the requirement of reducing reflection waves at the top boundary with a reasonable absorbing-layer thickness.

5.2. Characteristic methods

The second is the Thompson-like approach [8,9,16] that is a characteristic method to relate the wave amplitudes on the free-space boundary to the temporal evolution of primitive variables on the boundary. Following Thompson's analysis [9], for the wave propagation problem in the y–z plane in the current study, the characteristic equations at the boundary located at $z = z_{\max}$ become

$$\begin{aligned}
&\frac{\partial p_a}{\partial t} + \frac{1}{2}(L_1 + L_2) + v_a \frac{\partial p_a}{\partial y} + \gamma p_a \frac{\partial v_a}{\partial y} = 0,\\
&\frac{\partial v_a}{\partial t} + L_3 + v_a \frac{\partial v_a}{\partial y} + \frac{1}{\rho_a}\frac{\partial p_a}{\partial y} = 0,\\
&\frac{\partial w_a}{\partial t} + \frac{1}{2\rho_a c}(L_4 - L_1) + v_a \frac{\partial w_a}{\partial y} = 0,
\end{aligned} \tag{36}$$

where L_i represents the amplitude of each of the wave mode and can be expressed as

$$\begin{aligned}
L_1 &= \lambda_1\left(\frac{\partial p_a}{\partial z} - \rho_a c \frac{\partial w_a}{\partial z}\right),\\
L_2 &= \lambda_2\left(c_2 \frac{\partial \rho_a}{\partial z} - \frac{\partial p_a}{\partial z}\right),\\
L_3 &= \lambda_3 \frac{\partial v_a}{\partial z},\\
L_4 &= \lambda_4\left(\frac{\partial p_a}{\partial z} + \rho_a c \frac{\partial w_a}{\partial z}\right),
\end{aligned} \tag{37}$$

where λ_i is the velocity of the wave with the expressions

$$\begin{aligned}\lambda_1 &= w_a - c,\\ \lambda_2 &= \lambda_3 = w_a,\\ \lambda_3 &= w_a + c.\end{aligned} \tag{38}$$

In the above equations, the subscript "a" represents a total variable in the air that includes both of the average and acoustic parts. It can be seen in Eqs. (37) and (38) that mode 1 is the incoming sound wave to the boundary at $z_{\max}$, modes 2 and 3 are, respectively, the entropy and advection modes, and mode 4 is the outgoing sound wave at $z_{\max}$. If all the primitive variables are constant along the y-direction, Eq. (36) reduces to the local one-dimensional inviscid (LODI) system of Poinsot and Lele [17].

For the non-reflecting boundary condition, Thompson [8,9] suggested to let the incoming sound wave amplitude be zero (perfectly non-reflecting) and the other characteristic wave amplitudes be computed as in Eq. (37) using one-sided derivative approximations. However, it was found that the perfectly non-reflecting boundary condition, which is specified as $L_1 = 0$, led to an ill-posed condition in solving the Navier–Stokes equations in [17]. A modified condition for the incoming sound wave amplitude proposed in [17] is used in the present computation as

$$L_1 = K(p_a - p_{\text{av}}) = Kp, \tag{39}$$

where

$$K = \xi(1 - M_{\max}^2)c/h, \tag{40}$$

where $M_{\max}$ is the maximum Mach number of flow in the domain, h is the vertical size of the computational domain of the air which is 4 m in the test problem, and ξ is chosen to be 0.25 as in [17].

Since only the incoming wave amplitude, L_1, is determined with Eq. (39), the other three L_i are not changed and released back to the original equations. Consequently, the boundary equations at the top boundary of $z_{\max}$ are obtained, by using the modified non-reflecting incoming wave condition in the original wave equations in the air equations (2) and (3), to become

$$\frac{\partial \mathbf{u}}{\partial t} + (\mathbf{u}_{\text{av}} \cdot \nabla)\mathbf{u} + (\mathbf{u} \cdot \nabla)\mathbf{u}_{\text{av}} + \alpha_{\text{av}} \nabla p + \alpha \nabla p_{\text{av}} + \mathbf{R} = 0, \tag{41}$$

$$\frac{\partial p}{\partial t} + \mathbf{u}_{\text{av}} \cdot \nabla p + \mathbf{u} \cdot \nabla p_{\text{av}} + \gamma p \nabla \cdot \mathbf{u}_{\text{av}} + \gamma p_{\text{av}} \nabla \cdot \mathbf{u} + S = 0, \tag{42}$$

where

$$\mathbf{R} = \left[\frac{w_{\text{av}} - c}{\rho_{\text{av}} c}\left(\frac{\partial p}{\partial y} - \rho_{\text{av}} c \frac{\partial w}{\partial y}\right) - \frac{L_1}{\rho_{\text{av}} c}, 0\right]$$

and

$$S = \frac{1}{2}L_1 - (w_{\text{av}} - c)\left(\frac{\partial p}{\partial y} - \rho_{\text{av}} c \frac{\partial w}{\partial y}\right).$$

In the case studied here, $w_{\text{av}} = 0$. When computing Eqs. (41) and (42) at the top boundary, the z-direction spatial derivatives are calculated from the interior points using one-sided space differences, while the y-direction spatial derivatives are still calculated using the forward–backward scheme to be consistent with the calculation for the interior points. The same two-step explicit Euler time stepping is used for time marching.

5.3. Perfectly-matched layer absorbing boundary conditions

The concept of perfectly-matched layer (PML) was first formulated for electromagnetic radiation problems [10] and extended to the linearized Euler equations by Hu [11]. Recently, a formulation of PML for linearized Euler equations with non-uniform flows is proposed by Hu [18]. Here, we use the formulation for the unbounded boundary developed in [18] by adding a z-layer of PML above $z_{\max}$. Readers are referred to [18] for a complete derivation and explanation of the PML equations. In our study with a constant-shear velocity in the y-direction, the background velocity in the z-layer PML is uniform, equal to $V = V_{\text{av}}(z_{\max})$. Following [18], we rewrite the formulation for the application of the z-layer PML in this study as

$$\frac{\partial \mathbf{u}}{\partial t} + V\frac{\partial \mathbf{u}}{\partial y} + (\mathbf{u}\cdot\nabla)\mathbf{u}_{\text{av}} + \alpha_{\text{av}}\nabla p = -\zeta_z\left[V\frac{\partial \mathbf{q}}{\partial y} + (\mathbf{q}\cdot\nabla)\mathbf{u} + \mathbf{u} + \alpha_{\text{av}}\nabla q_p\right], \tag{43}$$

$$\frac{\partial p}{\partial t} + V\frac{\partial p}{\partial y} + \mathbf{u}\cdot\nabla p_{\text{av}} + \gamma p_{\text{av}}\nabla\cdot\mathbf{u} = -\zeta_z\left[\gamma p_{\text{av}}\frac{\partial q_v}{\partial y} + V\frac{\partial q_p}{\partial y} + p\right], \tag{44}$$

where the auxiliary variables in this problem are $\mathbf{q} = (q_v, q_w)$ and q_p. They are defined as

$$\frac{\partial \mathbf{q}}{\partial t} \equiv \mathbf{u}, \tag{45}$$

$$\frac{\partial q_p}{\partial t} \equiv p. \tag{46}$$

The absorption coefficient, ζ_z, varies with z as

$$\zeta_z = \zeta_{\max}\left|\frac{z - z_{\max}}{D}\right|, \tag{47}$$

where D is the width or height of the PML domain, and different values of $\zeta_{\max}$ have been tested and the results are presented in the next subsection.

One can notice that the equations in the PML, Eqs. (43) and (44), are the same as the sound propagation equations when the absorbing coefficient is set to zero. Hence, the same backward–forward numerical scheme described previously is implemented to compute the PML equations. The right-hand side of these equations are calculated at the previous time step so that the explicit scheme is used. The auxiliary variables in Eqs. (45) and (46) are computed using a simple first-order forward time differencing.

5.4. Comparisons of computational results

In the following computational results, the time step is $\Delta t = 0.01$ ms, and the space grid sizes are $\Delta y = 0.02$ m and $\Delta z = 0.02$ m, except at $z \in [-0.5, 0.5]$ where $\Delta z = 0.005$ m. These sizes are the same as used in [2], except that absorbing layers at the top boundary of the domain were not considered in that work.

Figs. 3a–d are sound pressure contours at $t = 15$ ms under different boundary and background flow conditions. Fig. 3a is for rigid top boundary without ambient flow. In this case, at the top boundary at $z = 4$, the rigid boundary condition is specified. This case is the same case as shown in Fig. 3 in [2], and the agreement with their result at 15 ms is very good. It shows that the primary wave (the strongest wave) is followed by a reflection from the ground boundary. When these two waves reach the top boundary, which is a rigid-surface boundary in this case, each of them generates a reflection wave. Since the ground is a porous medium with a finite resistivity, a sound wave transmitted into the ground is also shown for $z \in [-1, 0]$. This wave decays fast in the ground medium because of the high resistivity, with only a very weak reflection wave shown at $z = -1$ where the rigid boundary condition is specified.

Fig. 3b is the same case as Fig. 3a, except that a simple porous absorbing layer, as discussed in Section 5.1 with a relatively thick layer of 1.5 m, is added to the top boundary, changing the domain size to $z \in [-1, 5.5]$.

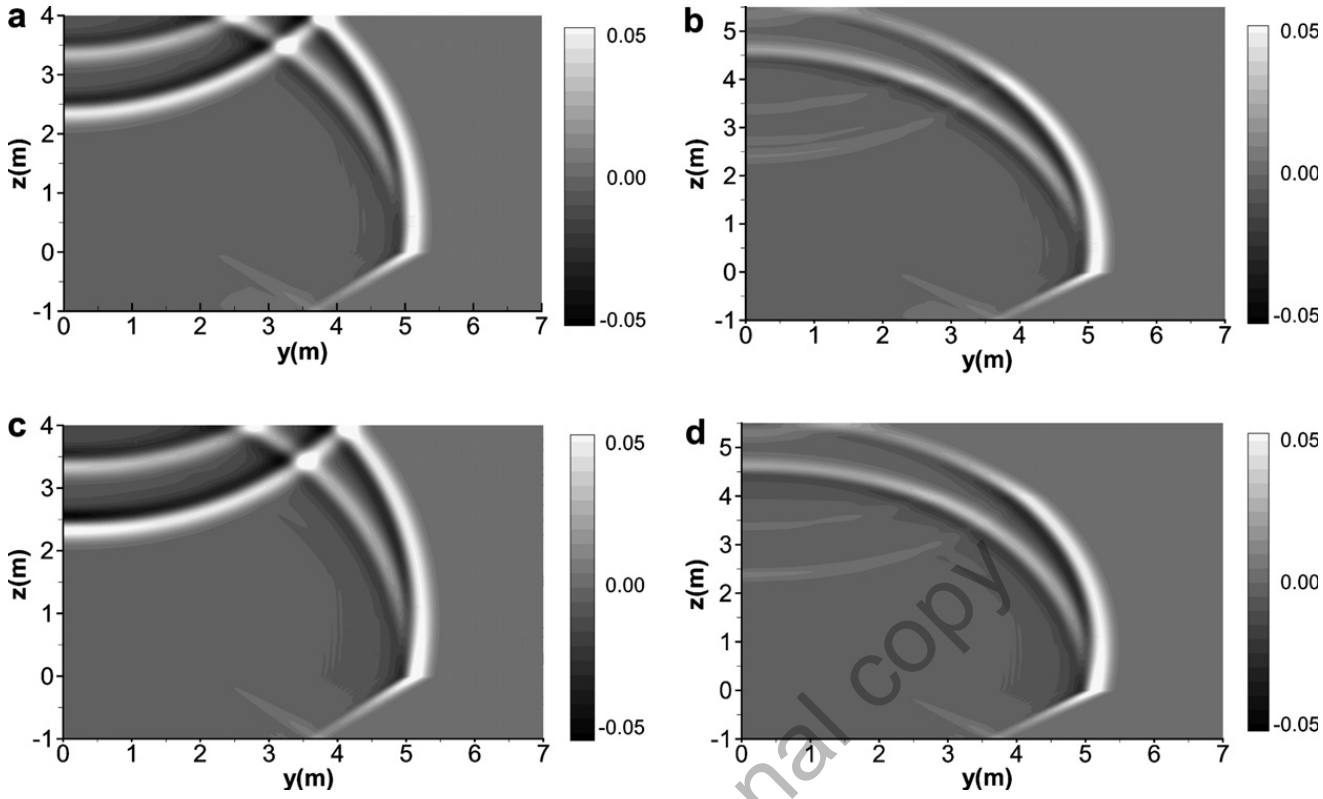

Fig. 3. Pressure contours at $t = 15$ ms. (a) Rigid top boundary without ambient flow. (b) Porous absorbing top boundary without ambient flow. (c) Rigid top boundary with ambient flow, $V_{av} = 3z$. (d) Porous absorbing top boundary with ambient flow, $V_{av} = 3z$.

The flow resistivity in this absorbing layer is selected as 1 kPa s m^{-2}. At the end of the porous layer ($z = 5.5$), a rigid boundary condition is specified. The results in Fig. 3b show that strong reflection waves at $z = 4$ in Fig. 3a are now replaced by two weak reflection waves. The incident waves at the top boundary ($z = 4$) are allowed to propagate outward. This situation approximates a free-space boundary condition at the top boundary with a reasonable accuracy.

Figs. 3c and d are the corresponding rigid-boundary and simple-porous-layer cases with ambient flow. The ambient flow is specified as $V_{av} = 3z$ where z is in m and V_{av} is in m/s. The absorbing-layer condition still works well with the ambient flow, and the similar discussions for Figs. 3a and b apply to Figs. 3c and d, too. However, by comparing Fig. 2d with Fig. 2b, relatively stronger reflections are observed in Fig. 3d. This means under the influence of shear flow, the simple porous absorbing layer does not work as well as in the homogeneous case.

A more detailed comparison for sound propagation is facilitated by placing a sound receiver at (5, 1.5), a location where the reflection waves from the top boundary do not reach within the simulation time (20 ms). The purposes are twofolds: to compare with results in [2] and to investigate if adding an absorbing layer would influence the signal at the receiver (which physically should not). Figs. 4a and b are the plots of relative sound pressure levels versus frequency for cases without and with ambient flow respectively. The ambient flow has again a velocity profile of $V_{av} = 3z$. The data of Salomons et al. [2] are from their Figs. 4 and 6. Notice again that their computation used the staggered grid, while ours uses the collocated grid. Also, in their study, the top boundary at $z = 4$ was treated as a rigid boundary only. It can be seen that a perfect agreement among those results has been achieved. The rigid-boundary and the simple-absorbing-boundary results are almost identical, with only slight differences between the staggered grid and collocated grid results at the higher frequency range. Note that the receiver is outside the influence region of the reflection waves. Obviously, if the reflection waves propagated through the receiver position, differences between the rigid-boundary and absorbing-boundary cases would show.

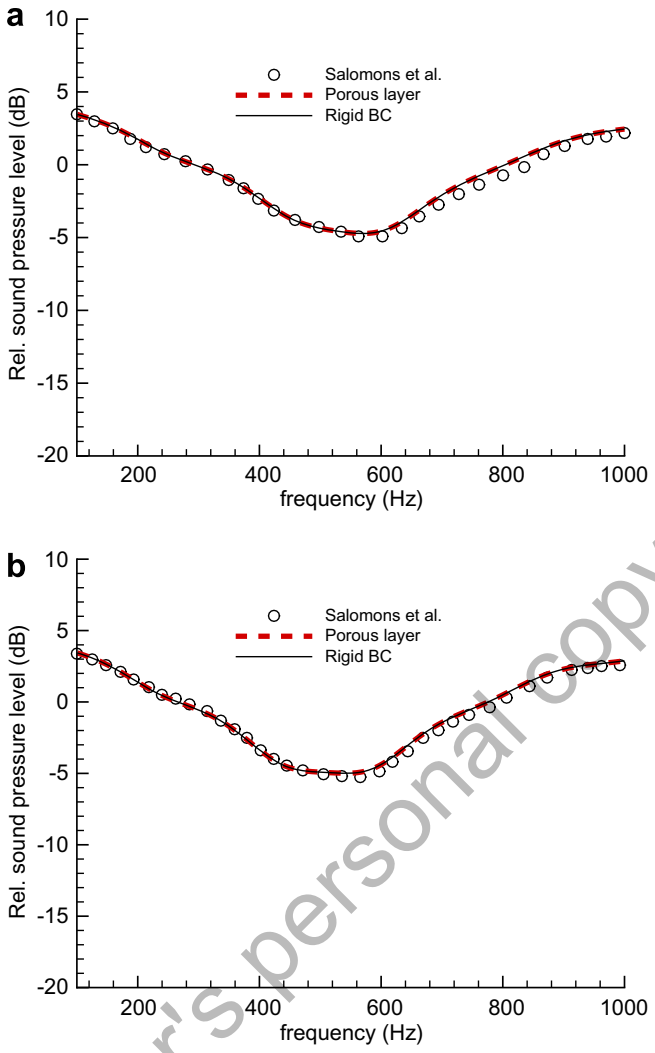

Fig. 4. Comparisons of relative sound pressure levels versus frequency at the location of the sound receiver in a region without influence of the reflection waves from the top boundary: (a) without ambient flow and (b) with ambient flow, $V_{\text{av}} = 3z$.

In the above simulation, the absorbing layer is relatively thick, more than 1/3 of the original domain height, which increases computational cost significantly. Furthermore, even with such a thick porous layer, reflection waves are still discernible. In the following test cases, we compare the behaviors of non-reflective boundary conditions.

Fig. 5 is used to address the effect of boundary conditions by comparing the numerical results with the analytical solution shown in [2] for the homogeneous case (without the background flow). The source is again placed at $(0, 0.5)$, the same position as in the previous cases. The position of the receiver changes at the height of 1.5 m and 3 m above the ground, going through the lateral position from 0 m to 12 m. These position ranges are from a 34-ms simulation, which cover both of the influenced region and the non-influenced region of the reflection waves from the top boundary. The relative sound pressure levels versus the position in Fig. 5 are plotted at two different frequencies, 300 Hz and 1000 Hz. The analytical solution uses the Helmholtz equation [2] for free-space sound propagation above the ground. Three different boundary conditions are compared: a characteristic boundary condition (CBC) at $z_{\max}$, as discussed in Section 5.2; a porous layer boundary condition at $z_{\max}$, with CBC at the end of the porous layer at z_e; a PML at $z_{\max}$, with CBC at the end of the porous layer at z_e. In both the porous layer and the PML cases, the thickness of the extra absorbing layer is reduced to 0.6 m, resulting in $z_e = 4.6$. In the porous layer, the flow resistivity is selected as 0.8 kPa sm^{-2}. In the PML, $\zeta_{\max} = 5000$ 1/s.

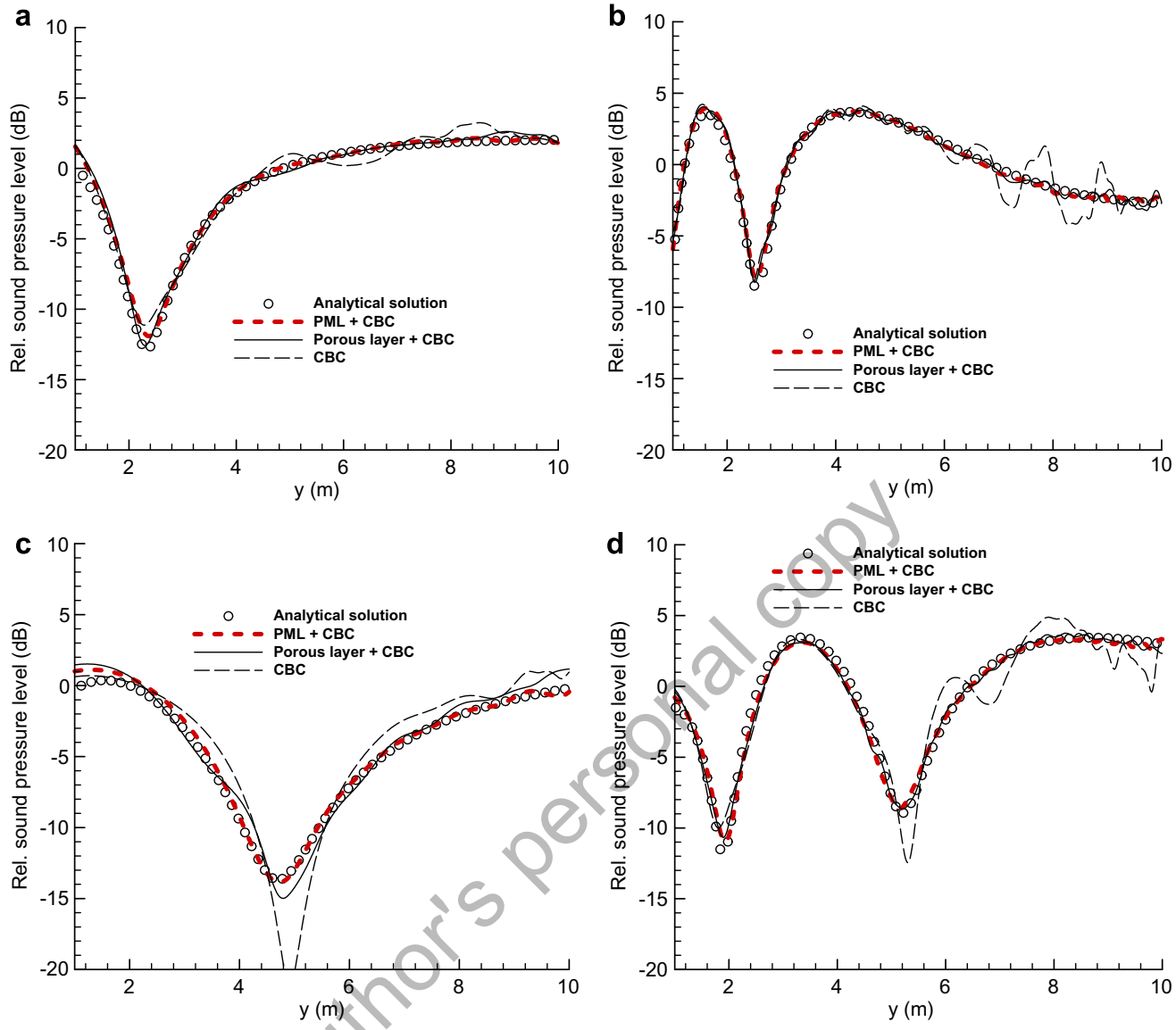

Fig. 5. Comparisons of relative sound pressure levels versus receiver position at two different heights and two different frequencies for simulations with non-reflecting boundary conditions at the top boundary under homogeneous (no ambient flow) atmosphere: (a) at $z = 1.5$ m and frequency 300 Hz, (b) at $z = 1.5$ m and frequency 100 Hz, (c) at $z = 3$ m and frequency 300 Hz, and (d) at $z = 3$ m and frequency 1000 Hz.

Fig. 5 shows that in all the cases, the results of the PML with the CBC match the analytical solution very well. The results from the porous layer with CBC are also good. The CBC only boundary condition, which does not require an extra absorbing layer and therefore is the cheapest in the computational cost among the three, unfortunately gives the worst results, particularly at the high frequency where excessive wiggles are generated. Only in the region of approximately $y < 4$, the CBC results agree with the others because there is no reflection in this region.

Fig. 6 is for the same comparisons as in Fig. 5 for the non-homogeneous case, with the background flow $V_{\text{av}} = 3z$. With the background flow, analytical solutions are not found. Therefore, the solution of a larger domain size in the z-direction extended to $z_{\max} = 6.4$ is used for comparison. In the large-domain solution, only the rigid wall boundary condition is used at $z_{\max} = 6.4$ without using any of the non-reflective boundary conditions. With the large domain, the reflection waves from the top boundary, due to the rigid wall boundary condition, do not reach to the regions of the solution to be compared after 34 ms of simulation time.

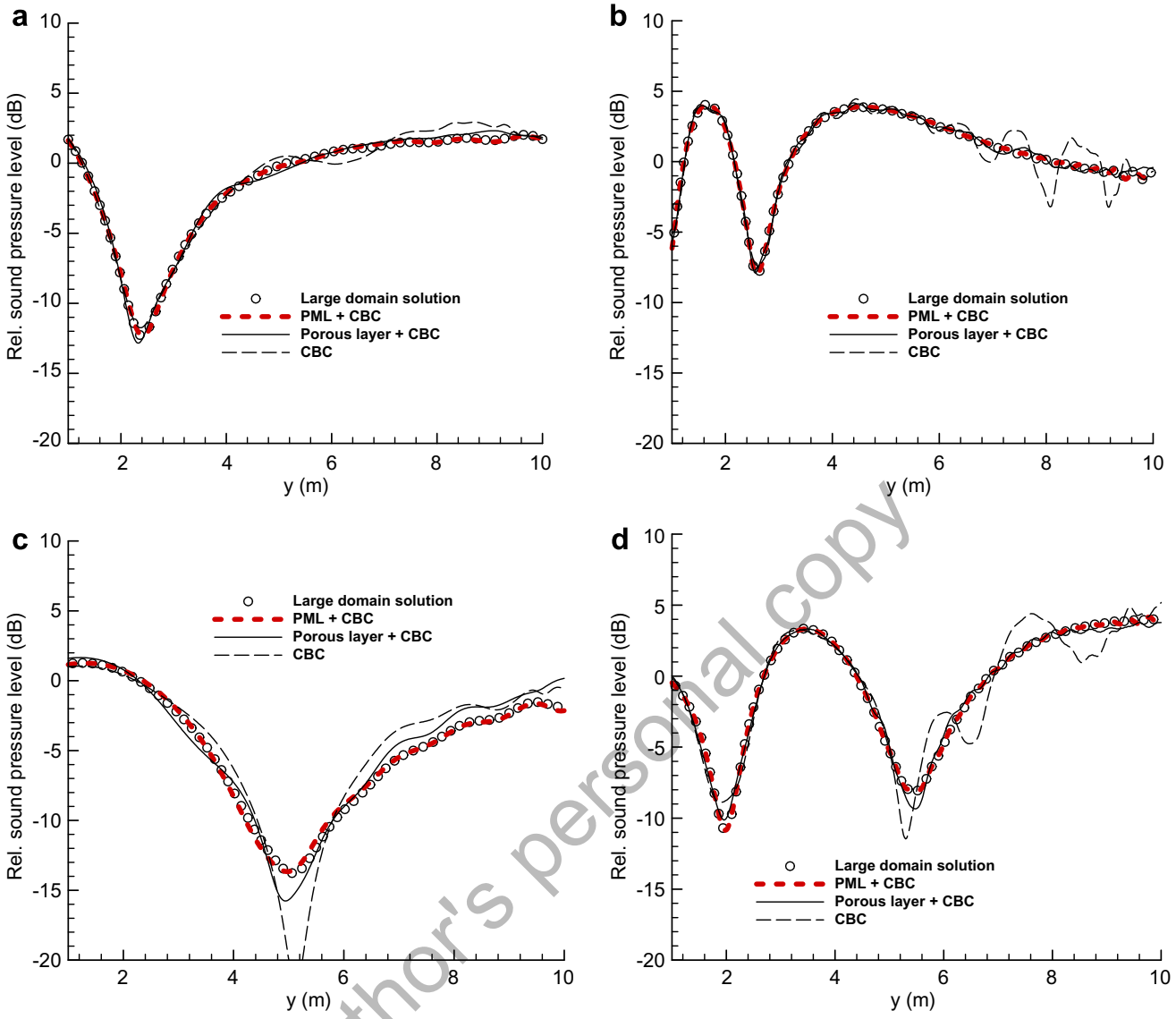

Fig. 6. Comparisons of relative sound pressure levels versus receiver position at two different heights and two different frequencies for simulations with non-reflecting boundary conditions at the top boundary under non-homogeneous atmosphere with $V_{av} = 3z$: (a) at $z = 1.5$ m and frequency 300 Hz, (b) at $z = 1.5$ m and frequency 100 Hz, (c) at $z = 3$ m and frequency 300 Hz, and (d) at $z = 3$ m and frequency 1000 Hz.

The solution in these regions is thus considered a solution without influence of boundary conditions specified at the top boundary. Fig. 6 shows that the same conclusion about the boundary condition behaviors can be made. That is, the PML with CBC shows the best results in comparison to the large-domain solution, and the CBC-only boundary condition shows the worst.

It is noted that in the above results, CBC boundary conditions are used at the end of either the porous layer or the PML (at z_e). The necessity of doing so is further explained by pressure contours shown in Fig. 7 with either the CBC or the rigid boundary condition specified at the end of PML, for the same non-homogeneous case as in Fig. 6. It also shows that the selection of proper ζ_{max} (or flow resistivity, σ, in the case of a porous layer) also influences the effectiveness of the absorbing layer. In Fig. 7, two types of the end boundary conditions are used, rigid and CBC; and two values of ζ_{max} are tested, 5000 1/s and 40,000 1/s. It can be seen that Fig. 7c shows no reflection waves, under the condition of $\zeta_{max} = 5000$ 1/s and CBC at the end of PML. A higher ζ_{max} value, although absorbs wave better, may generate reflection at the interface between the PML and the flow medium.

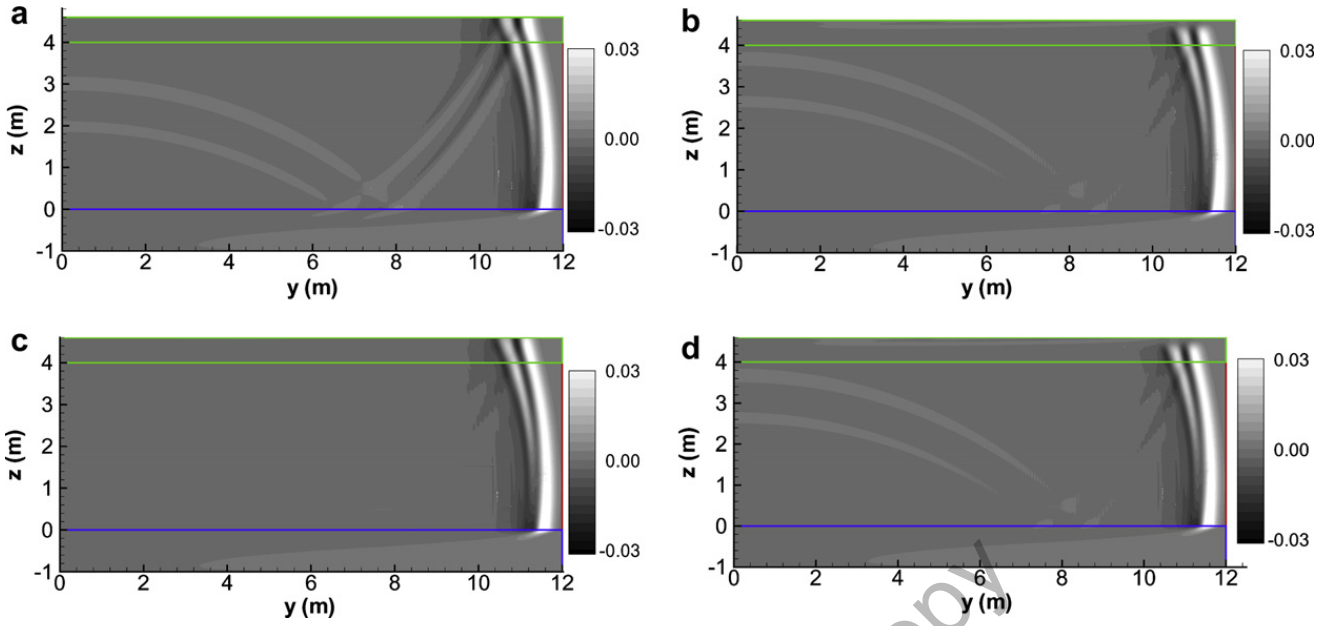

Fig. 7. Pressure contours at $t = 34$ ms with the PML boundary condition at z_{max} under non-homogeneous atmosphere with $V_{av} = 3z$: (a) $\zeta_{max} = 5000$ 1/s, rigid boundary at z_e, (b) $\zeta_{max} = 40,000$ 1/s, rigid boundary at z_e, (c) $\zeta_{max} = 5000$ 1/s, CBC at z_e, (d) $\zeta_{max} = 40,000$ 1/s, CBC at z_e.

6. Conclusion

Alternating of forward differencing and backward differencing on a collocated grid results in equivalent central differencing schemes on a staggered grid. Therefore the same stability condition using the von Neumann stability analysis applies to both of the computational grids. The stability condition shows that there is an upper limit on the flow resistivity of the porous medium for the computational scheme to be stable. The computational results using the collocated grid have shown good agreement with the literature data and analytical solution. The non-reflecting boundary conditions used to effectively represent the free-space condition have been tested. According to the results, the perfectly-matched layer method combining with the characteristic boundary condition specified at the end of the absorbing layer provides the best results. Proper selections of the absorbing coefficient are also necessary to achieve no reflections.

References

[1] R. Blumrich, D. Heimann, A linearized Eulerian sound propagation model for studies of complex meteorological effects, J. Acoust. Soc. Am. 112 (2002) 446–455.
[2] E.M. Salomons, R. Blumrich, D. Heimann, Eulerian time-domain model for sound propagation over a finite-impedance ground surface. Comparison with frequency-domain models, Acta Acust. 88 (2002) 483–492.
[3] D.K. Wilson, L. Liu, Finite-difference, time-domain simulation of sound propagation in a dynamic atmosphere, Private communication, 2003.
[4] S.V. Patankar, Numerical Heat Transfer and Fluid Flow, McGraw-Hill, New York, 1980.
[5] Z.E.A. Fellah, C. Depollier, Transient acoustic wave propagation in porous rigid media: a time-domain approach, J. Acoust. Soc. Am. 107 (2000) 683–688.
[6] I. Orlanski, A simple boundary condition for unbounded hyperbolic flows, J. Comput. Phys. 21 (1976) 251–269.
[7] B. Enquist, A. Majda, Absorbing boundary conditions for the numerical simulation of waves, Math. Comput. 31 (139) (1977) 629–651.
[8] K.W. Thompson, Time dependant boundary conditions for hyperbolic systems, J. Comput. Phys. 68 (1987) 1–24.
[9] K.W. Thompson, Time dependant boundary conditions for hyperbolic systems II, J. Comput. Phys. 89 (1990) 439–461.
[10] J.P. Berenger, A perfectly matched layer for the absorption of electromagnetic waves, J. Comput. Phys. 114 (1994) 185–200.
[11] F.Q. Hu, On absorbing boundary conditions for linearized Euler equations by a perfectly matched layer, J. Comput. Phys. 129 (1996) 201–219.
[12] C. Zwikker, C.W. Kosten, Sound Absorbtion Materials, Elsevier, Amsterdam, 1949.

[13] P.M. Morse, K.U. Ingard, Theoretical Acoustics, McGraw-Hill, New York, 1968.
[14] V.W. Sparrow, R. Raspet, A numerical method for general finite amplitude wave propagation in two dimensions and its application to spark pulses, J. Acoust. Soc. Am. 90 (1991) 2683–2691.
[15] D.A. Anderson, J.C. Tannehill, R.H. Pletcher, Computational Fluid Mechanics and Heat Transfer, McGaw-Hill, New York, 1984.
[16] R. Berthet, D. Astruc, Numerical boundary conditions for sound scattering simulation, J. Comput. Phys. 190 (2003) 64–69.
[17] T.J. Poinsot, S.K. Lele, Boundary conditions for direct simulations of compressible viscous flows, J. Comput. Phys. 101 (1992) 104–129.
[18] F.Q. Hu, A perfectly matched layer absorbing boundary condition for linearized Euler equations with a non-uniform mean-flow, J. Comput. Phys. 208 (2005) 469–492.